

Reconstructing 3D Flow from 2D Data with Diffusion Transformer

Fan Lei
Institute of Artificial Intelligence
Xiamen University

February 6, 2025

Abstract

Fluid flow is a widely applied physical problem, crucial in various fields. Due to the highly nonlinear and chaotic nature of fluids, analyzing fluid-related problems is exceptionally challenging. Computational fluid dynamics (CFD) is the best tool for this analysis but involves significant computational resources, especially for 3D simulations, which are slow and resource-intensive. In experimental fluid dynamics, PIV cost increases with dimensionality. Reconstructing 3D flow fields from 2D PIV data could reduce costs and expand application scenarios. Here, We propose a Diffusion Transformer-based method for reconstructing 3D flow fields from 2D flow data. By embedding the positional information of 2D planes into the model, we enable the reconstruction of 3D flow fields from any combination of 2D slices, enhancing flexibility. We replace global attention with window and plane attention to reduce computational costs associated with higher dimensions without compromising performance. Our experiments demonstrate that our model can efficiently and accurately reconstruct 3D flow fields from 2D data, producing realistic results.

1 Introduction

Fluid flow is perhaps the most widely applied physical problem to date, from the design of aerospace vehicle wings [54], to optimizing the output rate of chemical reactors, to analyzing pollutant dispersion [25] and wastewater treatment in environmental issues. Due to the highly nonlinear and chaotic nature of fluids, analyzing fluid-related problems becomes exceptionally challenging. Analytically solving the Navier-Stokes equations, which determine the essence of fluid behavior, remains an impossible task [52].

Computational fluid dynamics (CFD) is the best tool for analyzing fluid flow. It uses numerical methods and computer simulations to solve fluid problems. A typical CFD simulation process involves generating a mesh, i.e., dividing a geometric model into small discrete elements, setting boundary and initial conditions, and solving the Navier-Stokes equations to obtain flow field data.

Although CFD can simulate fluid flow quite accurately in most cases, it involves a significant investment of computational resources, especially for simulations in 3D space, and very slow. Common methods to reduce computational resource consumption include performing calculations only on half (or even a quarter) of the geometric model, assuming the model is highly symmetrical, or performing calculations in 2D space, using information from the 2D space to describe fluid flow characteristics in 3D space. These approaches involve strong assumptions that partial information of the flow field can capture the overall fluid flow characteristics and may require extensive specialized knowledge and manual effort. However, these assumptions may not always hold. Therefore, we often need to perform CFD simulations in 3D space to fully capture the fluid flow characteristics in the entire 3D space.

In the field of experimental fluid dynamics, particle-image velocimetry (PIV) [1, 58, 59] is a key method for obtaining flow field information. PIV uses high-speed cameras to capture particle images during laser pulses, recording particle positions in the flow field. Algorithms compare the particle distribution in different frames to find the distance particles move within the time interval, thereby calculating the velocity vector at each point in the flow field and generating velocity field data. The cost of PIV technology is also affected by dimensionality. For example, 3D3C PIV requires more high-speed cameras than 2D3C PIV to capture velocity field data in 3D space. Therefore, if 3D flow fields can be reconstructed from 2D PIV data, it will greatly reduce costs and expand the application scenarios of PIV technology.

The large amount of flow data obtained from numerical simulations and experiments directs our attention to data-driven methods. In the field of fluid dynamics, machine learning, especially deep learning methods [32], has made significant progress [5, 31, 71, 13, 72], from improving measurement techniques based on machine learning [19, 20] to accelerating numerical solution methods [66, 50], surrogate models [47, 75], flow field prediction and reconstruction [76, 35, 12], and flow control [14, 21]. Machine learning methods have shown strong application potential, with deep learning models accurately modeling highly nonlinear and chaotic fluids, making them an ideal choice for reconstructing 3D flow fields. Although deep learning models usually require a long training process, once trained, their inference speed can be several orders of magnitude faster than traditional numerical methods.

On the other hand, the vigorous development of generative models [61, 23, 62, 10, 55] and the research progress in 3D reconstruction tasks [16, 43, 44, 24, 26] make it possible to reconstruct the 3D flows from some partial observations (such as 2D flow field). In this paper, we demonstrate that the state-of-the-art generative model has strong generative capabilities, it trained with flow data to acquire sufficient prior knowledge about the flow field, can recover the entire 3D flow field information from partial flow field information, thereby obtaining the flow characteristics of the 3D flow field. Specifically, we trained a Transformer-based Diffusion model [70, 23, 51], integrating plane position embeddings to capture the spatial information of 2D planes while utilizing window and plane attention mechanisms to handle the computational complexity

of three-dimensional flows. This design enables the reconstruction of 3D flow fields from 2D flow data, with the plane position embeddings allowing the model to recover 3D flow information from arbitrary combinations of 2D planes.

In summary, the contributions of this paper are:

- We propose a method for reconstructing the 3D flow field from partial flow data, e.g., 2D flow observations, leveraging the strong prior knowledge of a trained diffusion model.
- We replace vanilla global attention with the simpler yet highly effective window attention and plane attention to alleviate the increased computational cost brought by higher dimensions. Our results demonstrate that these new attention mechanisms can significantly reduce computational costs with minimal impact on model performance.
- By embedding the position information of 2D planes into the model, we enable the recovery of 3D flow fields through any 2D plane combination, effectively utilizing training data and enhancing the flexibility of 3D flow field reconstruction.
- We demonstrate through experiments that our model can successfully reconstruct 3D flow fields from 2D flow field data, capturing the true distribution of the flow field and generating realistic samples.

2 Related Work

Flow Prediction and Reconstruction. Flow prediction focuses on forecasting flow behavior at future time steps based on domain geometry, boundary, and initial conditions. Although numerical solvers offer high accuracy, they are computationally expensive, with resource demands escalating rapidly in higher dimensions, driving the search for more efficient alternatives. Hybrid methods leverage data-driven models to replace costly components of numerical solvers, while purely machine learning approaches, such as neural networks, directly predict flow fields. Neural operators [2, 67, 30, 34, 33, 22] exemplify this by learning functional mappings for flow prediction. Other works applying deep learning to flow field prediction include [27, 35, 12]. Additionally, incorporating physical constraints into models [53, 74] has proven to enhance prediction accuracy. Flow field reconstruction, in contrast, seeks to recover the full 3D flow field from partial observations, leveraging the model’s prior knowledge of the underlying flow dynamics. Matsuo et al. [41] and Yousif et al. [76] are the most relevant to our work. Matsuo et al. [41] utilized CNNs to reconstruct 3D flow fields from multiple parallel 2D sections, while Yousif et al. [76] employed a GAN-based approach to recover 3D flow fields from two orthogonal 2D flow fields. Unlike their approaches, we employ a powerful generative model, the diffusion model, combined with a Transformer architecture. Additionally, unlike their methods, which recover 3D flow fields from fixed-position 2D planes, we introduce a novel

plane position embedding, allowing the model to reconstruct 3D flow fields from different combinations of 2D planes.

3D Reconstruction. Recent advancements in computer vision have significantly enhanced 3D reconstruction techniques [16, 43, 44, 38, 60, 26, 46, 49, 79], with promising applications for 3D flow field reconstruction. Neural Radiance Fields (NeRFs) [44, 24, 9] generate 3D scenes by training neural networks on multiple 2D images to produce color and density outputs. Generative models further advance this field by directly creating 3D representations from 2D images [37] or synthesizing novel views [38, 60, 46] to support 3D scene reconstruction [73]. Additionally, significant progress has been made in Gaussian splatting [49, 26, 77] and implicit representations [65, 68, 78, 79]. Among these methods, the most relevant to our 3D flow field reconstruction is the generative model-based approach. However, instead of generating novel object views from images, we reconstruct the corresponding 3D flow field from provided 2D flow field slices. In this work, we represent the 3D flow field as voxels and reconstruct it from 2D slices. Common 3D representations include point clouds [69, 48, 42, 6], meshes [39, 36, 16], and voxels [15, 57, 45]. Of these, voxel-based techniques are particularly relevant to this approach. However, other 3D representations may also provide viable solutions for flow field reconstruction.

Diffusion Models. Generative models, particularly diffusion models [61, 23, 62], have advanced rapidly, emerging as state-of-the-art in generation quality and diversity. They now outperform other generative frameworks, such as variational autoencoders (VAEs) [29], autoregressive models (ARMs) [8], flow-based models [11], and generative adversarial networks (GANs) [17]. Diffusion models have shown great potential across fields, with recent applications to 3D data [6, 45, 73, 48, 60, 46]. While U-Nets [56] have traditionally served as the backbone for diffusion models, Transformer-based architectures are gaining traction [70]. DiT [51] employs a pure Transformer backbone, demonstrating impressive scalability. Extensions like DiT-3D [45], U-ViT [3], and UniDiffuser [4] further explore Transformers in diffusion models. Given their success, we selected Transformers for reconstructing 3D flows. To manage the computational complexity of 3D spatial data, we replaced global attention with plane and window attention. These linear-complexity attention mechanisms introduce inductive biases by leveraging the locality of flow fields, enhancing efficiency without sacrificing expressive power.

3 Method

3.1 Preliminaries

In this subsection, we first introduce the problem setting of reconstructing 3D flow fields from 2D flow fields. Then, we briefly provide some background knowledge on denoising diffusion probabilistic models (DDPMs). Finally, we describe two-stage approach and CFG, explaining our reasons for not using them.

Problem Setup. For a given set of 2D slices $P = \{p_i\}_{i=1}^n$ within a 3D flow field, each 2D slice $p_i \in \mathbb{R}^{d_1 \times d_2 \times c}$, where c represents flow field attributes such as pressure or velocity, our goal is to reconstruct the 3D flow field $S \in \mathbb{R}^{d_x \times d_y \times d_z \times c}$. We aim to learn f_θ , a neural network parameterized by θ ,

$$\hat{S} = f_\theta(P, E_P), \quad (1)$$

as a function of the 2D plane set P and the plane position embedding E_P (section 3.2), and outputs the reconstructed 3D flow field \hat{S} . We want \hat{S} to be as similar as possible to S .

To create f_θ for reconstructing the flow field with high quality, we need to address two key issues. First, reconstructing a 3D flow field from 2D slices is very challenging, as it is an ill-posed problem that involves inferring global information from local data and requires strong prior knowledge. The second question is how do we address the potentially enormous computational costs associated with 3D data? For the first problem, we chose a generative model with sufficient generalization capabilities—a diffusion transformer. It learns the prior knowledge about flow fields from the training data, as introduced in section 3.3. For the second question, we addressed it by replacing the traditional attention mechanism with more computationally efficient window attention and plane attention mechanisms. Furthermore, to enhance the flexibility of flow field reconstruction, we propose the plane position embedding, discussed in section 3.2, which allows us to fully utilize the 3D data.

Background on Diffusion Models. Diffusion Models define the forward process as a Markov chain, which incrementally injects noise into the original data. The reverse process is also a Markov chain, continuously removing noise from a certain prior distribution to recover the original data. The essence of Diffusion Models lies in learning this reverse process.

For the original 3D flow field data S_0 , the forward process continuously adds noise, generating S_1, S_2, \dots, S_T . The typical form of the transition kernel is usually $q(S_t|S_{t-1}) = \mathcal{N}(S_t; \sqrt{1 - \beta_t}S_{t-1}, \beta_t\mathbf{I})$, where $\beta_t \in (0, 1)$ is a Gaussian noise value.

For the backward process, The reverse Markov chain is characterized by a transition kernel $p_\theta(S_{t-1}|S_t) = \mathcal{N}(S_{t-1}; \mu_\theta(S_t, t), \Sigma_\theta(S_t, t))$, where θ denotes model parameters. For training, we can form variational upper bound [29] which reduces to $\mathcal{L}(\theta) = -p(S_0|S_1) + \sum_t D_{KL}(q(S_{t-1}|S_t, S_0)||p_\theta(S_{t-1}|S_t))$. Given that both $q(S_t|S_0)$ and $p_\theta(S_{t-1}|S_t)$ are Gaussian, and considering that the backward process operates conditioned on the 2D flow field and its corresponding positional embedding, we can simplify the training objective to

$$\mathcal{L}_{simple}(\theta) = \mathbb{E}_{t, S_0, \epsilon} \|\epsilon - \epsilon_\theta(S_t, c(t, P, E_P))\|_2^2 \quad (2)$$

where $c(t, P, E_P)$ is the condition of timestep, 2D flow field and plane position embedding. Once $p_\theta(S_{t-1}|S_t)$ is trained, the model f_θ can reconstruct the 3D flow field S_0 by applying iterative denoising conditioned on $c(t, P, E_P)$.

Two-stage Approach and CFG. Due to the substantial computational resources required to train diffusion models in high-resolution pixel/voxel space,

LDM [55] employs a two-stage approach to address this issue: (1) Train a high-quality autoencoder and use its encoder E to map the data S to a lower-dimensional latent space. (2) Freeze the autoencoder and train the diffusion model in the latent space to restore the latent representation of the raw data from Gaussian noise z_T to $z_0 = E(x)$. After model training is completed, we can sample in the latent space and use the decoder to obtain the original data $S = D(Z)$.

LDM can achieve better 3D flow field reconstruction with fewer computational resources. However, we did not use it for two reasons: (1) There is no off-the-shelf autoencoder trained on 3D flow field data. (2) Training a 3D autoencoder for 3D flow from scratch requires a large amount of high-quality flow field data and computational resources. Training a diffusion model directly in the voxel space is less costly. Therefore, we have set training the autoencoder as a task for future work.

Classifier-free guidance (CFG) is commonly used in conditional diffusion models. According to Bayes Rule, $\log p(c|x) \propto \log p(x|c) - \log p(x)$, so $\nabla_x \log p(c|x) \propto \nabla_x \log p(x|c) - \nabla_x \log p(x)$. Here, c represents conditional information, such as 2D flow information. Through reparameterization, $\hat{\epsilon}_\theta(x_t, c) = \epsilon_\theta(x_t, \emptyset) + s \cdot \nabla_x \log p(x|c) \propto \epsilon_\theta(x_t, \emptyset) + s \cdot (\epsilon_\theta(x_t, c) - \epsilon_\theta(x_t, \emptyset))$, where $s > 1$ is the guidance scale, \emptyset represents unconditional generation. By this, we can sample from $p(x|c)$ to obtain x under the condition c . However, we found in experiments that the reconstruction results of the model are highly sensitive to s . Therefore, to achieve accurate 3D flow reconstruction and avoid hyperparameter tuning, we did not use CFG.

3.2 Plane Position Embedding

To enable the model to reconstruct 3D flow fields from any combination of 2D flow fields, we input both the features of the two-dimensional flow fields and their position embedding into the model. We use a Cartesian coordinate system to describe the spatial relationships within the flow field. For convenience, we normalize the coordinates of each point in 3D flow field to be contained inside the XYZ unit cube $[0, 1]^3$. Consider the equation of planes $Ax + By + Cz + D = 0$, we normalize it by dividing by $\mathbf{n} = \sqrt{A^2 + B^2 + C^2}$, resulting in $A'x + B'y + C'z + D' = 0$. We do not consider planes where $D' > 1$, thereby ignoring planes that intersect the cube $[0, 1]^3$ with a small area. Instead of directly inputting the four values A' , B' , C' , and D' into the model, we feed them into the model via Fourier feature embeddings. This approach enriches the features and provides a continuous and smooth representation of plane equation.

Specifically, for the given dimension d , and plane equation parameter A' , the embedding can be represented as

$$\text{PE}(A', 2i) = \sin\left(A'/10000^{(2i/d)-1}\right), \quad (3)$$

$$\text{PE}(A', 2i + 1) = \cos\left(A'/10000^{(2i/d)-1}\right). \quad (4)$$

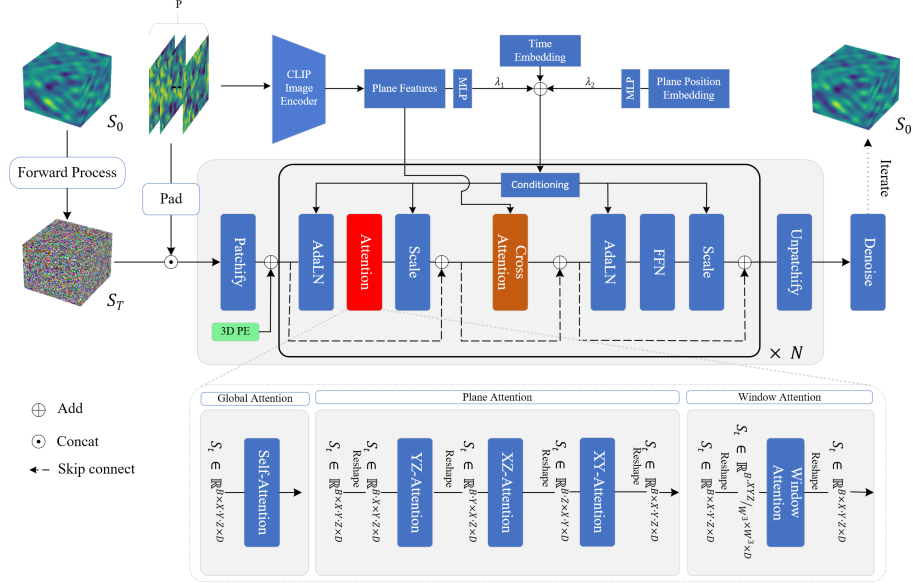


Figure 1: **Pipeline and architecture.** We use the Diffuse Transformer to reconstruct 3D flow from 2D flow. **Top:** The 2D flow is fed into the model through three paths: 1) it is padded and concatenated with the input; 2) features are extracted using CLIP, combined with the timestep embedding and plane position embedding, and used as conditioning; and 3) the final layer output of the CLIP image encoder is fed into the model via cross-attention. **Middle:** The structure of the Diffuse Transformer. The input flow field undergoes patchification, passes through N transformer layers, and is unpatchified to produce the predicted noise in the flow field. Global attention is replaced with more efficient window attention and plane attention within the transformer. **Bottom:** The structure of different attention mechanisms. Both window attention and plane attention are implemented through reshaping operations.

where i is the dimension index. Note that since A' , B' , C' , and D' are less than 1, we multiply them by 10,000. Consequently, in Equation (3) and (4), the exponent of the numerator becomes $(2i/d) - 1$ instead of the usual $2i/d$. We concatenate the embeddings of the four plane equation parameters to obtain the positional embeddings $E_{p_i} = [\text{PE}(A'_i), \text{PE}(B'_i), \text{PE}(C'_i), \text{PE}(D'_i)]$ for each plane p_i . We then concatenate these to form the overall plane positional embedding $E_P = [E_{p_1}, \dots, E_{p_n}]$, project it to the model dimension D using a multi-layer perceptron (MLP), add it to the timestep embedding t_{emb} , and feed the result into the model.

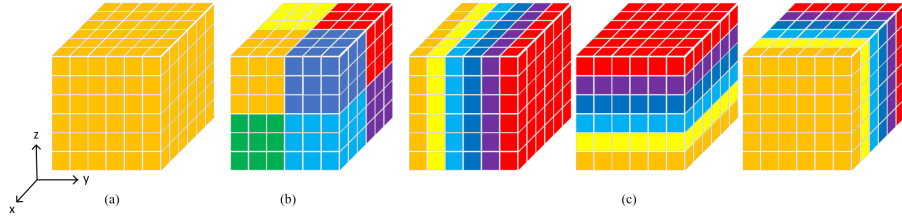


Figure 2: **Visual explanation of different attention.** Each grid of the cube represents an input token, and only tokens of the same color can attend to each other. (a) Global attention. (b) Window attention. (c) Plane attention: from left to right, yOz plane attention, xOz plane attention, and xOy plane attention.

3.3 Diffusion Transformer for 3D Flow Field Reconstruction

Inspired by recent works [45, 51, 7], we use a diffusion transformer to reconstruct 3D flow from 2D. The 3D flow field is converted into input tokens through a 3D patchify operation, and 3D positional embeddings are added before processing the tokens through N transformer layers, which utilize window and plane attention. The 2D flow features are extracted using CLIP which are input to the model through adaptive layer norm. Finally, a linear layer and an unpatchify operation output the predicted noise in the 3D flow. The entire pipeline and architecture are shown in Figure 1.

3D Patchify. The typical Transformer architecture processes data of shape $B \times L \times D$, where B denotes the batch size, L is the sequence length, and D is the dimension of the model. However, we treat the 3D flow field as voxels, $S \in \mathbb{R}^{d_x \times d_y \times d_z \times c}$. Therefore, the first layer of our model is designed to patchify S . For a patch size of $p_x \times p_y \times p_z$, we use a 3D convolution layer with both kernel size and stride set to the patch size. This layer converts the input flow field voxels into a sequence of 3D patchified tokens $T_S \in \mathbb{R}^D$ with sequence length $L = X \cdot Y \cdot Z = \frac{d_x}{p_x} \cdot \frac{d_y}{p_y} \cdot \frac{d_z}{p_z}$. The patch size does not impact the number of parameters in the model but affects the size of L , which is the attention window size in the transformer. Changes in patch size influence L and model’s flops and, consequently, the quality of flow reconstruction [51]. Next, we add 3D positional embeddings [45] to the input tokens based on the spatial position of the corresponding voxels.

Transformer Layers. Each transformer layer contains a self-attention layer, a cross-attention layer, and a feed-forward layer. The self-attention is defined as $\text{attention}(x_i) = \text{softmax}\left(\frac{\mathbf{Q}\mathbf{K}^T}{\sqrt{D}}\right)\mathbf{V}$, where $\mathbf{Q} = x_i\mathbf{W}^{\mathbf{Q}}$, $\mathbf{K} = x_i\mathbf{W}^{\mathbf{K}}$, and $\mathbf{V} = x_i\mathbf{W}^{\mathbf{V}}$. $\mathbf{W}^{\mathbf{Q}}$, $\mathbf{W}^{\mathbf{K}}$, $\mathbf{W}^{\mathbf{V}} \in \mathbb{R}^{D \times D}$ are parametric projection matrices, and D denotes the input token dimension. Finally, the output is passed through a linear layer and added to the residual connection

$$\text{SelfAttn}(x_i) = \text{Linear}(\text{attention}(x_i)) + x_i. \quad (5)$$

To alleviate the computational cost increase brought by 3D processing, we replace vanilla global attention with window attention or plane attention. Figure 2 provides a visual explanation of these operations.

For window attention, we use a window size of $w \times w \times w$, reducing the input token sequence length L to w^3

$$x_i = \text{Reshape}(B \cdot \frac{L}{w^3}, w^3, D)(x_i), \quad (6)$$

where x_i is the input tokens, $\text{Reshape}(B \cdot \frac{L}{w^3}, w^3, D)$ denotes dividing the original L input tokens into $\frac{L}{w^3}$ groups, each of length w^3 , where attention operations are performed only within each group of w^3 tokens. Since the time complexity of the attention operation is quadratic in the input token length, the Reshape operation reduces the time complexity from $O(L^2)$ to $O(Lw^3)$. In our experiments, $w = 4$, thus reducing the time complexity by a factor of 8 (with $L = 512$).

For plane attention, similar to window attention, we group tokens based on their spatial positions

$$x_i = \text{Reshape}(B \cdot \frac{L}{X}, Y \cdot Z, D)(x_i), \quad (7)$$

where $\text{Reshape}(B \cdot \frac{L}{X}, Y \cdot Z, D)$ ensures that tokens only in the yOz plane can attend to each other. Note that tokens in the yOz plane may correspond to multiple flow fields because of the 3D patchify operation at the beginning of the model. In one self-attention sub-layer, we repeat plane attention three times, corresponding to the yOz , xOz , and xOy planes, as shown in Figure 2. These simple modifications to vanilla attention operation introduce inductive biases into the model, leveraging the locality of flow fields to enhance computational efficiency while maintaining performance.

Following the self-attention, cross-attention is applied to incorporate the 2D flow field information. Additionally, AdaLN and Scale, as shown in Figure 1, also serve as methods for injecting flow field information, which we will describe in detail later. The final feed-forward network (FFN) consists of two linear layers with an activation function in between, similar to [70].

Conditioning. We adopted a triple-stream conditioning mechanism. In the first stream, we pad the 2D flow field to 3D to align with the model’s input, then channel-concatenate it with the 3D flow field being denoised. This approach directly feeds the detailed information from the 2D flow field into the model, ensuring that the local details of the reconstructed flow field align with the corresponding 2D slices.

For the second conditioning stream, we use CLIP’s image encoder to extract features F_{p_i} for all 2D planes p_i in the set P . These features are concatenated to form the plane feature embedding F_P , which is then projected to the dimension of the input tokens using an MLP. Next, the timestep embedding t_{emb} and plane position embedding E_P are added to obtain the conditional information embedding

$$c(t, P, E_P) = t_{emb} + \lambda_1 F_P + \lambda_2 E_P, \quad (8)$$

where λ_1 and λ_2 are two learnable weight parameters, both initialized to 1. Note that we use the global semantic token from the 2D flow field, specifically CLIP’s class token \mathbf{f}_{cls} , to capture its global features. Following DiT [51], we input the conditional information embedding c into the model through adaptive layer norm.

Assuming x_i is a sequence of vectors in the i -th sub-layer of the Transformer, adaLN with embedding c is defined as

$$\text{adaLN}_i(x_i) = (1 + \gamma_i) \cdot \text{LN}(x_i) + \beta_i, \quad (9)$$

$$\beta_i, \gamma_i = \text{MLP}_i^{\text{Scale, Shift}}(c), \quad (10)$$

where γ_i and β_i are the scale and shift parameters, and LN is the layer normalization. adaLN is applied to each sub-layers of the Transformer layer.

Additionally, a scale α_i output by another MLP is applied to x_i prior to the residual connections in each sub-layer

$$\text{Scale}_i(x_i) = \alpha_i \cdot x_i, \quad (11)$$

$$\alpha_i = \text{MLP}_i^{\text{Scale}}(c). \quad (12)$$

We zero-initialize these MLPs to accelerate training [18].

Although the global token effectively represents the information of the flow field, it cannot capture the full extent of the flow. To provide more comprehensive flow information to the model, we use the CLIP image encoder’s final layer output $\mathbf{F}_{\text{last}} = \{\mathbf{f}^i\}_{i=1}^K$ as input for the third conditioning stream via cross-attention. This output has been proven to offer high-fidelity representations in numerous studies.

4 Experiments

4.1 Experimental Setup

Datasets. In our experiments, we primarily focus on two different datasets, corresponding to the incompressible Navier-Stokes (INS) equations and the compressible Navier-Stokes (CNS) equations.

The incompressible Navier-Stokes equations are a simplified version of the original equations, assuming that the fluid density is independent of pressure. The equations are given by

$$\nabla \cdot \mathbf{u} = 0, \rho \left(\frac{\partial \mathbf{u}}{\partial t} + \mathbf{u} \cdot \nabla \mathbf{u} \right) = -\nabla p + \mu \nabla^2 \mathbf{u} + \mathbf{f} \quad (13)$$

where \mathbf{u} is the velocity, ρ is the density, p is the internal pressure, and \mathbf{f} represents external forces. We use a dataset from [76], consisting of a turbulent channel flow at friction Reynolds numbers $Re_\tau = 180$.

The compressible Navier-Stokes equations are expressed as

$$\frac{\partial \rho}{\partial t} + \nabla \cdot (\rho \mathbf{u}) = 0, \quad (14)$$

$$\rho\left(\frac{\partial \mathbf{u}}{\partial t} + \mathbf{u} \cdot \nabla \mathbf{u}\right) = -\nabla p + \eta \nabla^2 \mathbf{u} + (\zeta + \eta/3) \nabla(\nabla \cdot \mathbf{u}), \quad (15)$$

$$\partial\left(\epsilon + \frac{\rho u^2}{2}\right)/\partial t + \nabla \cdot \left[\left(\epsilon + p + \frac{\rho u^2}{2}\right) \mathbf{u} - \mathbf{u} \cdot \sigma'\right] = 0, \quad (16)$$

where $\epsilon = p/(\Gamma - 1)$ is the internal energy density, $\Gamma = 5/3$, σ' is the stress tensor, and η, ζ are the shear and bulk viscosity, respectively. Our dataset is from [64], with shear viscosity η of 1×10^{-8} and bulk viscosity ζ of 1×10^{-8} , Mach number as 1.0, and turbulence initial conditions.

Both datasets are generated using direct numerical simulation (DNS). For the INS dataset, we employ two different data partitioning methods to test the model’s interpolation and extrapolation capabilities, denoted as INS(INT) and INS(EXT), respectively. Specifically, each flow field in the INS dataset has a corresponding time step. For INS(INT), we randomly split data from different time steps into training and test sets, whereas for INS(EXT), we use data from the first 80% of time steps for training and the remaining time steps for testing. Since $\Delta t = 0.07$, the flow fields at consecutive time steps are similar, allowing INS(INT) to evaluate the model’s ability to reconstruct 3D flow fields when ample data is available. In contrast, INS(EXT) assesses the model’s generalization capability across different time steps. For the CNS dataset, we only test the model’s extrapolation capability. In addition, we also test our model’s capability to reconstruct flow fields around geometric objects (Section 4.4).

Metrics. We use normalized root-mean-square error (nRMSE) measure the accuracy of the 3D flow field reconstruction

$$\text{nRMSE} = \frac{\|u_{pred} - u_{true}\|_2}{\|u_{true}\|_2}, \quad (17)$$

and use the peak signal-to-noise ratio (PSNR) to assess the quality of the reconstructed 2D slices of the flow field

$$\text{PSNR} = 10 \cdot \log_{10} \frac{\text{MAX}^2(u_{true})}{\text{MSE}(u_{true}, u_{pred})}. \quad (18)$$

We also adapt the structural similarity index measure (SSIM) to better assess the detailed aspects of the reconstructed flow field

$$\text{SSIM} = \frac{(2\mu_{u_{true}}\mu_{u_{pred}} + C_1)(2\sigma_{u_{true}u_{pred}} + C_2)}{(\mu_{u_{true}}^2 + \mu_{u_{pred}}^2 + C_1)(\sigma_{u_{true}}^2 + \sigma_{u_{pred}}^2 + C_2)}, \quad (19)$$

where C_1 and C_2 are constants, which we set to 0.01 and 0.03, respectively. We calculate SSIM with a local window of $11 \times 11 \times 11$.

Implementations. We implemented three different model sizes: Small, Base, and Large. Table 1 gives details of our models. Note that only some of the global attention in the model are replaced with window attention or plane attention.

We reconstruct the 3D velocity field u, v, w . The model uses the AdamW [28, 40] optimizer. The learning rate is set to 1×10^{-4} and we use a Cosine-Annealing-LR scheduler. The batch size is 32, and we train for 10,000 epochs.

Table 1: Details of models. (*) denotes models that use window attention and plane attention.

MODEL	LAYERS N	HIDDEN SIZE D	HEADS	WINDOW ATTN LAYER	PLANE ATTN LAYER
SMALL	8	384	6	N/A	N/A
SMALL*	8	384	6	(1,4)	(2,5)
BASE	10	648	8	N/A	N/A
BASE*	10	648	8	(1,4,7)	(2,5,8)
LARGE	12	768	12	N/A	N/A
LARGE*	12	768	12	(1,4,7,10)	(2,5,8,11)

4.2 Baselines

We briefly introduce the baseline models compared in the experiments, with detailed descriptions provided in the Appendix.

F-FNO. The Fourier Neural Operator (FNO) [34] is a model designed for solving partial differential equations (PDEs) by learning mappings between infinite-dimensional function spaces. It leverages Fourier transforms to operate in the frequency domain, enabling efficient handling of complex continuous dynamical systems. The Factorized FNO (F-FNO) [67] introduces improvements over the original FNO, particularly in terms of model depth, to enhance its scalability. In our experiments, we used a 24-layer F-FNO with 16 Fourier modes and 64 channels.

U-Net-mod. We compared with U-Net-mod, an improved architecture based on the traditional U-Net, designed to accommodate more complex tasks. The modifications in U-Net-mod includes a deeper network, more sophisticated convolutional kernels, alternative upsampling strategies, and the incorporation of novel regularization methods and attention mechanisms.

Dil-ResNet. The dilated ResNet (Dil-ResNet) is proposed by Stachenfeld et al. [63] as a neural PDE solver, it achieves a larger receptive field with fewer convolution operations compared to traditional ResNet. However its speed is significantly slower. Therefore, we limited our model to an 8-layer Dil-ResNet with 64 channels, where each layer consists of seven 3D convolutions with dilation rates of [1, 2, 4, 8, 4, 2, 1].

For all baseline models, we padded 2D planes to three dimensions as input, with the corresponding 3D flow as output. MSE is employed as the loss function. Additionally, we report the performance of the 2D3DGAN proposed by Yousif et al. [76] on the INS dataset.

4.3 Results

Table 2 shows the test results of the baseline models and our proposed method on three datasets. All models reconstruct the 3D flow field from two orthogonal 2D flow field planes. Figure 3 presents visualizations of flow fields reconstructed

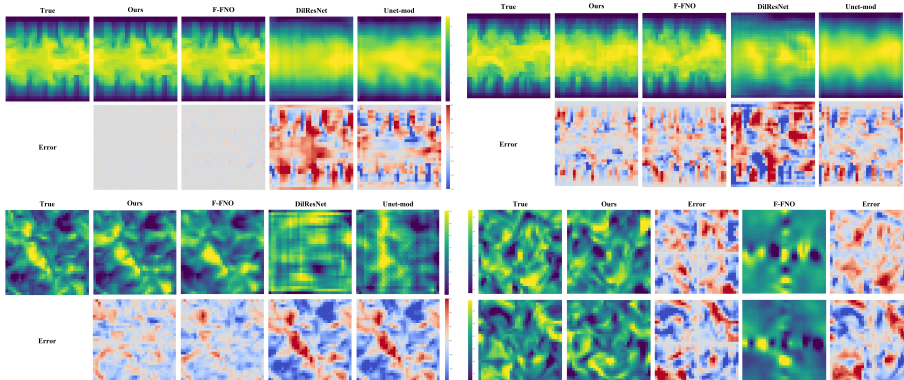


Figure 3: Visualization of results from different models on the INS(INT) (top left), INS(EXT) (top right), CNS (bottom left), and CNS xOy planes where the reference xOy plane is not provided. Note that the displayed 2D flow fields are not the inputs to the models.

by different models, with the flow field planes taken from planes adjacent to the reference 2D planes used for reconstruction.

Across all three metrics, our method achieves the best results on all datasets, especially on the INS(INT) dataset. This demonstrates that when the training data covers all flow field information, our method can very accurately reconstruct the 3D flow field from 2D observations. Based on the metrics, our Large model may exhibit overfitting, likely due to the lack of measures to prevent overfitting, such as dropout. In terms of flow field visualization, other methods generally fail to reconstruct the detailed information of the flow field, which is also evident from the SSIM metric. Surprisingly, the flow field reconstructed by F-FNO also appears highly realistic and is not much worse than ours.

In the other two datasets, where we test the model’s extrapolation capability, nearly all models show a decline in test metrics. Although our method does not outperform others significantly in these metrics, its lead in SSIM indicates superior reconstruction of flow field details, which is corroborated by the visualized results.

Additionally, as shown in the bottom right of Figure 3, when flow field information for a specific 2D plane, such as the xOy plane, is not provided, F-FNO fails to reconstruct the corresponding flow field, resulting in meaningless noise. In contrast, while our method may not achieve the same accuracy as when plane information is available, it can still reconstruct a meaningful flow field.

We plotted three different test metrics of the model’s reconstruction results across three planes (xOy , yOz , xOz) on the INS(INT) dataset, as shown in Figure 4. The relative position indicates the plane’s location relative to the 2D plane used for reconstruction, i.e., the center of the XYZ cube. We can see that our model maintains high reconstruction quality across different spatial positions, although the reconstruction results on the yOz plane show slight fluctuations.

Table 2: Summary of the three test metrics on different datasets. An asterisk (*) denotes models that use window attention and plane attention. The best performance is shown in bold.

MODEL	INS(INT)			INS(EXT)			CNS		
	nRMSE(\downarrow)	PSNR(\uparrow)	SSIM(\uparrow)	nRMSE(\downarrow)	PSNR(\uparrow)	SSIM(\uparrow)	nRMSE(\downarrow)	PSNR(\uparrow)	SSIM(\uparrow)
F-FNO	0.0352	39.8618	0.9630	0.1421	22.4728	0.7966	0.1230	24.2100	0.7969
UNET-MOD	0.1267	23.4915	0.7861	0.1245	23.6319	0.7860	0.1233	24.8443	0.7517
DILRESNET	0.1354	22.8427	0.7740	0.1651	21.2144	0.7424	0.1250	24.7098	0.7423
2D3DGAN	0.3630	-	-	-	-	-	-	-	-
SMALL (OURS)	0.0653	29.1077	0.9567	0.1298	22.9346	0.8132	0.1225	24.4753	0.8349
BASE (OURS)	0.0053	51.0158	0.9997	0.1331	22.9346	0.8105	0.1180	24.8012	0.8410
LARGE* (OURS)	0.0121	43.7522	0.9992	0.1229	23.7372	0.8119	0.1154	25.0022	0.8361

Figure 5 presents the same three test metrics across three planes on the CNS dataset. It can be seen that our model reconstructs the flow field outward from the input 2D flow fields (reference flow fields). The closer the position of the 2D slices in the reconstructed 3D flow field is to the reference flow fields, the better the reconstruction effect. This is because the closer distance ensures more accurate flow field information provided by the reference flow fields. In contrast, at positions far from the reference flow fields, the reconstructed flow field has a larger error compared to the true values. This suggests that increasing the number of reference flow fields used for reconstruction and ensuring their even spatial distribution can improve the reconstruction quality of the flow field.

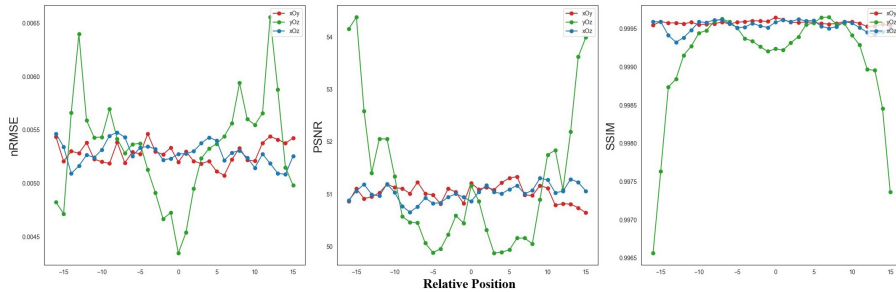


Figure 4: Relative positions to the center of the 3D flow field versus three test metrics on INS(INT).

4.4 Reconstructing the 3D flow around geometries

In addition to testing our model’s ability to reconstruct 3D channel turbulence, we also evaluated its performance in reconstructing flow fields around geometries. We used the 2x2-large dataset from [35], with the geometries in the dataset illustrated on the left side of Figure 6. Table 3 presents the model’s reconstruction results, while the right side of Figure 6 shows the corresponding visualizations. The results indicate that our model effectively handles flow fields around geometries, achieving high realism and accuracy in the reconstructions.

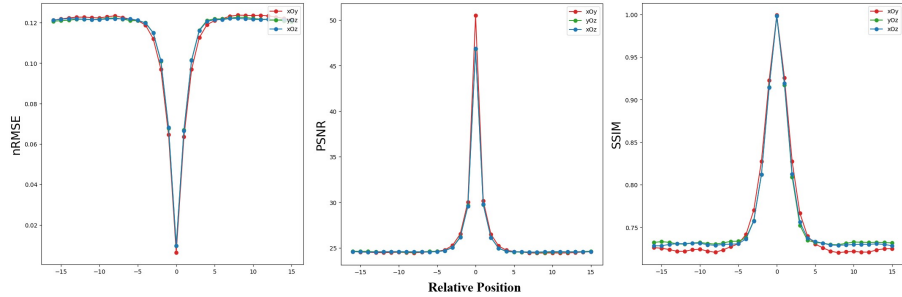


Figure 5: Relative positions to the center of the 3D flow field versus three test metrics on CNS.

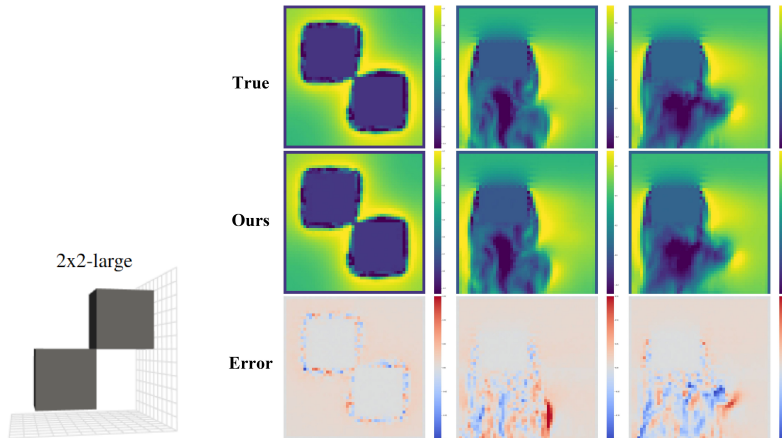


Figure 6: Visualization of reconstructing the 3D flow field around geometries. Left: 2x2 large object in dataset [35]. Right: results, the velocity field u .

Table 3: Corresponding metrics for the reconstruction results of the 3D flow around geometries.

MODEL	nRMSE(\downarrow)	PSNR(\uparrow)	SSIM(\uparrow)
LARGE*	0.1524	33.4711	0.9793

4.5 Ablation Study

In this section, we present the results of the ablation experiments.

Number of 2D Planes. Table 4 shows the impact of the number of 2D planes used for reconstructing the 3D flow field on reconstruction quality. Adding additional 2D planes does not significantly affect reconstruction quality. The Small and Large models showed no improvement with the increase in the number

of planes, while the Base model showed a slight improvement but a decrease in the SSIM. It is possible that adding just one more 2D flow field does not provide enough additional information and instead puts pressure on the model’s training optimization.

Table 4: Ablation study results on the number of planes used for reconstruction, with the best results within the same model size highlighted in bold.

MODEL	# PLANES	INS(EXT)		
		nRMSE(↓)	PSNR(↑)	SSIM(↑)
SMALL	2	0.1298	23.1500	0.8132
	3	0.1343	22.8565	0.7915
BASE	2	0.1331	22.9346	0.8105
	3	0.1290	23.2084	0.7975
LARGE*	2	0.1229	23.7372	0.8119
	3	0.1269	23.3493	0.8006

Attention. The test results for models using different attention mechanisms are shown in Table 5. Replacing some of the global attention in the model with window attention and plane attention resulted in at least a 25% improvement in training speed. For the Small and Base models, this led to a slight performance impact, while the performance of the Large model actually improved. These results validate that the attention mechanisms we adopted can significantly reduce computational costs with little to no impact on model performance.

Table 5: Ablation study results on different attention. Better results in the same model size are shown in bold.

MODEL	ATTENTION	INS(EXT)			TRAINING (Step/Sec)	RELATIVE PROMOTION (%)
		nRMSE(↓)	PSNR(↑)	SSIM(↑)		
SMALL	Global	0.1298	23.1500	0.8132	2.97	N/A
	Win&Plane	0.1389	22.5629	0.7887	3.80	27.9
BASE	Global	0.1331	22.9346	0.8105	1.50	N/A
	Win&Plane	0.1342	22.8624	0.7930	1.94	31.4
LARGE	Global	0.1274	23.3126	0.7972	1.12	N/A
	Win&Plane	0.1269	23.3493	0.8006	1.56	39.3

Plane Position Embedding. We use three 2D planes located at a relative position of -5 from the center of the flow field for reconstruction, with plane position embedding providing the positional information of the 2D planes to the model. Figure 7 shows the metrics for the reconstructed flow. It can be observed that the reconstruction quality is high for flow fields near the relative position of -5, demonstrating that our plane position embedding successfully enables the model to reconstruct 3D flow fields from 2D planes at different locations.

Pacth Size. Table 6 presents the ablation study results on patch size. It can be observed that a smaller patch size does not significantly improve the

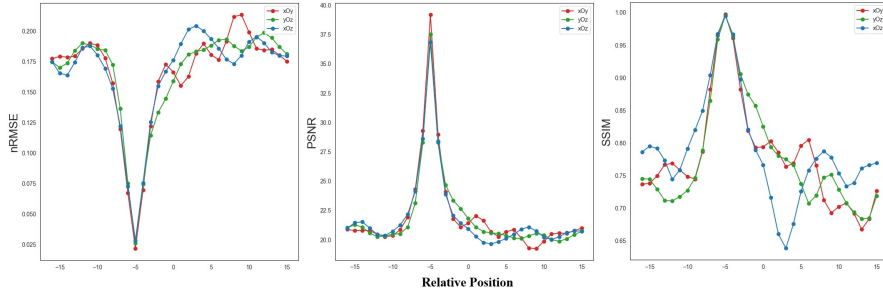


Figure 7: Relative positions to the center of the 3D flow field versus three test metrics. We use three 2D planes located at a relative position of -5 from the center of the flow field for reconstruction on CNS.

overall quality of the flow field but is effective in reconstructing the details of the flow field. We also found that the model fails to converge during training when the patch size is too large.

Table 6: Ablation study results on patch size. Experiment conducted on LARGE*. The model fails to converge when patch size is 8.

PATCH SIZE	CNS		
	nRMSE(↓)	PSNR(↑)	SSIM(↑)
2	0.1184	24.8302	0.8536
4	0.1154	25.0022	0.8361
8	N/A	N/A	N/A

5 Conclusion

In this work, we propose a Diffusion Transformer-based method for reconstructing 3D flow from 2D data. Additionally, we use plane position embeddings to provide the model with the positional information of the 2D flow fields, enabling the reconstruction of 3D flow from 2D flows at arbitrary locations, thereby enhancing reconstruction flexibility. By replacing conventional global attention with window attention and plane attention, we significantly reduce the computational costs associated with the increased token length from the additional dimension, without substantially compromising model performance. Our experiments demonstrate that our model can efficiently and accurately reconstruct 3D flow fields from 2D flow data, producing realistic 3D flows. However, our approach treats flows reconstruction as a generative task, ignoring the underlying physical significance. A potential future improvement could involve embedding the corresponding physical information of the flow into the model.

References

- [1] Ronald J Adrian. Scattering particle characteristics and their effect on pulsed laser measurements of fluid flow: speckle velocimetry vs particle image velocimetry. *Applied optics*, 23(11):1690–1691, 1984.
- [2] Anima Anandkumar, Kamyar Azizzadenesheli, Kaushik Bhattacharya, Nikola Kovachki, Zongyi Li, Burigede Liu, and Andrew Stuart. Neural operator: Graph kernel network for partial differential equations. In *ICLR 2020 Workshop on Integration of Deep Neural Models and Differential Equations*, 2020.
- [3] Fan Bao, Shen Nie, Kaiwen Xue, Yue Cao, Chongxuan Li, Hang Su, and Jun Zhu. All are worth words: A vit backbone for diffusion models. In *Proceedings of the IEEE/CVF conference on computer vision and pattern recognition*, pages 22669–22679, 2023.
- [4] Fan Bao, Shen Nie, Kaiwen Xue, Chongxuan Li, Shi Pu, Yaole Wang, Gang Yue, Yue Cao, Hang Su, and Jun Zhu. One transformer fits all distributions in multi-modal diffusion at scale. In *International Conference on Machine Learning*, pages 1692–1717. PMLR, 2023.
- [5] Steven L Brunton, Bernd R Noack, and Petros Koumoutsakos. Machine learning for fluid mechanics. *Annual review of fluid mechanics*, 52(1):477–508, 2020.
- [6] Wei Cao, Chang Luo, Biao Zhang, Matthias Nießner, and Jiapeng Tang. Motion2vecsets: 4d latent vector set diffusion for non-rigid shape reconstruction and tracking. In *Proceedings of the IEEE/CVF Conference on Computer Vision and Pattern Recognition*, pages 20496–20506, 2024.
- [7] Junsong Chen, YU Jincheng, GE Chongjian, Lewei Yao, Enze Xie, Zhongdao Wang, James Kwok, Ping Luo, Huchuan Lu, and Zhenguo Li. Pixart-alpha: Fast training of diffusion transformer for photorealistic text-to-image synthesis. In *The Twelfth International Conference on Learning Representations*.
- [8] Mark Chen, Alec Radford, Rewon Child, Jeffrey Wu, Heewoo Jun, David Luan, and Ilya Sutskever. Generative pretraining from pixels. In *International conference on machine learning*, pages 1691–1703. PMLR, 2020.
- [9] Congyue Deng, Chiyu Jiang, Charles R Qi, Xinchun Yan, Yin Zhou, Leonidas Guibas, Dragomir Anguelov, et al. Nerdi: Single-view nerf synthesis with language-guided diffusion as general image priors. In *Proceedings of the IEEE/CVF conference on computer vision and pattern recognition*, pages 20637–20647, 2023.
- [10] Prafulla Dhariwal and Alexander Nichol. Diffusion models beat gans on image synthesis. *Advances in neural information processing systems*, 34:8780–8794, 2021.
- [11] Laurent Dinh, David Krueger, and Yoshua Bengio. Nice: Non-linear independent components estimation. *arXiv preprint arXiv:1410.8516*, 2014.
- [12] Claudia Drygala, Francesca di Mare, and Hanno Gottschalk. Generalization capabilities of conditional gan for turbulent flow under changes of geometry. *arXiv preprint arXiv:2302.09945*, 2023.

- [13] Karthik Duraisamy, Gianluca Iaccarino, and Heng Xiao. Turbulence modeling in the age of data. *Annual review of fluid mechanics*, 51(1):357–377, 2019.
- [14] Dixia Fan, Liu Yang, Zhicheng Wang, Michael S Triantafyllou, and George Em Karniadakis. Reinforcement learning for bluff body active flow control in experiments and simulations. *Proceedings of the National Academy of Sciences*, 117(42):26091–26098, 2020.
- [15] Matheus Gadelha, Subhransu Maji, and Rui Wang. 3d shape induction from 2d views of multiple objects. In *2017 international conference on 3d vision (3DV)*, pages 402–411. IEEE, 2017.
- [16] Jun Gao, Tianchang Shen, Zian Wang, Wenzheng Chen, Kangxue Yin, Daiqing Li, Or Litany, Zan Gojcic, and Sanja Fidler. Get3d: A generative model of high quality 3d textured shapes learned from images. *Advances In Neural Information Processing Systems*, 35:31841–31854, 2022.
- [17] Ian Goodfellow, Jean Pouget-Abadie, Mehdi Mirza, Bing Xu, David Warde-Farley, Sherjil Ozair, Aaron Courville, and Yoshua Bengio. Generative adversarial networks. *Communications of the ACM*, 63(11):139–144, 2020.
- [18] Priya Goyal, Piotr Dollár, Ross Girshick, Pieter Noordhuis, Lukasz Wesolowski, Aapo Kyrola, Andrew Tulloch, Yangqing Jia, and Kaiming He. Accurate, large minibatch sgd: Training imagenet in 1 hour. *arXiv preprint arXiv:1706.02677*, 2017.
- [19] Luca Guastoni, Alejandro Güemes, Andrea Ianiro, Stefano Discetti, Philipp Schlatter, Hossein Azizpour, and Ricardo Vinuesa. Convolutional-network models to predict wall-bounded turbulence from wall quantities. *Journal of Fluid Mechanics*, 928:A27, 2021.
- [20] Alejandro Güemes, Stefano Discetti, Andrea Ianiro, Beril Sirmacek, Hossein Azizpour, and Ricardo Vinuesa. From coarse wall measurements to turbulent velocity fields through deep learning. *Physics of fluids*, 33(7), 2021.
- [21] Bing-Zheng Han and Wei-Xi Huang. Active control for drag reduction of turbulent channel flow based on convolutional neural networks. *Physics of Fluids*, 32(9), 2020.
- [22] Zhongkai Hao, Zhengyi Wang, Hang Su, Chengyang Ying, Yinpeng Dong, Songming Liu, Ze Cheng, Jian Song, and Jun Zhu. Gnot: A general neural operator transformer for operator learning. In *International Conference on Machine Learning*, pages 12556–12569. PMLR, 2023.
- [23] Jonathan Ho, Ajay Jain, and Pieter Abbeel. Denoising diffusion probabilistic models. *Advances in neural information processing systems*, 33:6840–6851, 2020.
- [24] Ajay Jain, Ben Mildenhall, Jonathan T Barron, Pieter Abbeel, and Ben Poole. Zero-shot text-guided object generation with dream fields. In *Proceedings of the IEEE/CVF conference on computer vision and pattern recognition*, pages 867–876, 2022.
- [25] Javier Jiménez. Near-wall turbulence. *Physics of Fluids*, 25(10), 2013.

- [26] Bernhard Kerbl, Georgios Kopanas, Thomas Leimkühler, and George Drettakis. 3d gaussian splatting for real-time radiance field rendering. *ACM Trans. Graph.*, 42(4):139–1, 2023.
- [27] Byungsoo Kim, Vinicius C Azevedo, Nils Thuerey, Theodore Kim, Markus Gross, and Barbara Solenthaler. Deep fluids: A generative network for parameterized fluid simulations. In *Computer graphics forum*, volume 38, pages 59–70. Wiley Online Library, 2019.
- [28] Diederik P Kingma and Jimmy Ba. Adam: A method for stochastic optimization. *arXiv preprint arXiv:1412.6980*, 2014.
- [29] Diederik P Kingma and Max Welling. Auto-encoding variational bayes. *arXiv preprint arXiv:1312.6114*, 2013.
- [30] Nikola Kovachki, Zongyi Li, Burigede Liu, Kamyar Azizzadenesheli, Kaushik Bhattacharya, Andrew Stuart, and Anima Anandkumar. Neural operator: Learning maps between function spaces with applications to pdes. *Journal of Machine Learning Research*, 24(89):1–97, 2023.
- [31] J Nathan Kutz. Deep learning in fluid dynamics. *Journal of Fluid Mechanics*, 814:1–4, 2017.
- [32] Yann LeCun, Yoshua Bengio, and Geoffrey Hinton. Deep learning. *nature*, 521(7553):436–444, 2015.
- [33] Zijie Li, Kazem Meidani, and Amir Barati Farimani. Transformer for partial differential equations’ operator learning. *arXiv preprint arXiv:2205.13671*, 2022.
- [34] Zongyi Li, Nikola Kovachki, Kamyar Azizzadenesheli, Burigede Liu, Kaushik Bhattacharya, Andrew Stuart, and Anima Anandkumar. Fourier neural operator for parametric partial differential equations. *arXiv preprint arXiv:2010.08895*, 2020.
- [35] Marten Lienen, David Lüdke, Jan Hansen-Palmus, and Stephan Günnemann. From zero to turbulence: Generative modeling for 3d flow simulation. In *The Twelfth International Conference on Learning Representations*.
- [36] Minghua Liu, Minhyuk Sung, Radomir Mech, and Hao Su. Deepmetahandles: Learning deformation meta-handles of 3d meshes with biharmonic coordinates. In *Proceedings of the IEEE/CVF Conference on Computer Vision and Pattern Recognition*, pages 12–21, 2021.
- [37] Minghua Liu, Ruoxi Shi, Linghao Chen, Zhuoyang Zhang, Chao Xu, Xinyue Wei, Hansheng Chen, Chong Zeng, Jiayuan Gu, and Hao Su. One-2-3-45++: Fast single image to 3d objects with consistent multi-view generation and 3d diffusion. In *Proceedings of the IEEE/CVF Conference on Computer Vision and Pattern Recognition*, pages 10072–10083, 2024.
- [38] Ruoshi Liu, Rundi Wu, Basile Van Hoorick, Pavel Tokmakov, Sergey Zakharov, and Carl Vondrick. Zero-1-to-3: Zero-shot one image to 3d object. In *Proceedings of the IEEE/CVF international conference on computer vision*, pages 9298–9309, 2023.

- [39] Zhen Liu, Yao Feng, Michael J Black, Derek Nowrouzezahrai, Liam Paull, and Weiyang Liu. Meshdiffusion: Score-based generative 3d mesh modeling. *arXiv preprint arXiv:2303.08133*, 2023.
- [40] Ilya Loshchilov and Frank Hutter. Decoupled weight decay regularization. *arXiv preprint arXiv:1711.05101*, 2017.
- [41] Mitsuaki Matsuo, Taichi Nakamura, Masaki Morimoto, Kai Fukami, and Koji Fukagata. Supervised convolutional network for three-dimensional fluid data reconstruction from sectional flow fields with adaptive super-resolution assistance. *arXiv preprint arXiv:2103.09020*, 2021.
- [42] Luke Melas-Kyriazi, Christian Rupprecht, and Andrea Vedaldi. Pc2: Projection-conditioned point cloud diffusion for single-image 3d reconstruction. In *Proceedings of the IEEE/CVF Conference on Computer Vision and Pattern Recognition*, pages 12923–12932, 2023.
- [43] Lars Mescheder, Michael Oechsle, Michael Niemeyer, Sebastian Nowozin, and Andreas Geiger. Occupancy networks: Learning 3d reconstruction in function space. In *Proceedings of the IEEE/CVF conference on computer vision and pattern recognition*, pages 4460–4470, 2019.
- [44] Ben Mildenhall, Pratul P Srinivasan, Matthew Tancik, Jonathan T Barron, Ravi Ramamoorthi, and Ren Ng. Nerf: Representing scenes as neural radiance fields for view synthesis. *Communications of the ACM*, 65(1):99–106, 2021.
- [45] Shentong Mo, Enze Xie, Ruihang Chu, Lanqing Hong, Matthias Niessner, and Zhenguo Li. Dit-3d: Exploring plain diffusion transformers for 3d shape generation. *Advances in neural information processing systems*, 36:67960–67971, 2023.
- [46] Norman Müller, Katja Schwarz, Barbara Rössle, Lorenzo Porzi, Samuel Rota Bulò, Matthias Nießner, and Peter Kotschieder. Multidiff: Consistent novel view synthesis from a single image. In *Proceedings of the IEEE/CVF Conference on Computer Vision and Pattern Recognition*, pages 10258–10268, 2024.
- [47] Taichi Nakamura, Kai Fukami, Kazuto Hasegawa, Yusuke Nabae, and Koji Fukagata. Convolutional neural network and long short-term memory based reduced order surrogate for minimal turbulent channel flow. *Physics of Fluids*, 33(2), 2021.
- [48] Alex Nichol, Heewoo Jun, Prafulla Dhariwal, Pamela Mishkin, and Mark Chen. Point-e: A system for generating 3d point clouds from complex prompts. *arXiv preprint arXiv:2212.08751*, 2022.
- [49] Michael Niemeyer, Fabian Manhardt, Marie-Julie Rakotosaona, Michael Oechsle, Daniel Duckworth, Rama Gosula, Keisuke Tateno, John Bates, Dominik Kaeser, and Federico Tombari. Radsplat: Radiance field-informed gaussian splatting for robust real-time rendering with 900+ fps. *arXiv preprint arXiv:2403.13806*, 2024.
- [50] Octavi Obiols-Sales, Abhinav Vishnu, Nicholas Malaya, and Aparna Chandramowlishwaran. Cfdnet: A deep learning-based accelerator for fluid simulations. In *Proceedings of the 34th ACM international conference on supercomputing*, pages 1–12, 2020.

- [51] William Peebles and Saining Xie. Scalable diffusion models with transformers. In *Proceedings of the IEEE/CVF International Conference on Computer Vision*, pages 4195–4205, 2023.
- [52] Stephen B Pope. Turbulent flows. *Measurement Science and Technology*, 12(11): 2020–2021, 2001.
- [53] Maziar Raissi, Paris Perdikaris, and George E Karniadakis. Physics-informed neural networks: A deep learning framework for solving forward and inverse problems involving nonlinear partial differential equations. *Journal of Computational physics*, 378:686–707, 2019.
- [54] István Z Reguly, Gihan R Mudalige, Carlo Bertolli, Michael B Giles, Adam Betts, Paul HJ Kelly, and David Radford. Acceleration of a full-scale industrial cfd application with op2. *IEEE Transactions on Parallel and Distributed Systems*, 27(5):1265–1278, 2015.
- [55] Robin Rombach, Andreas Blattmann, Dominik Lorenz, Patrick Esser, and Björn Ommer. High-resolution image synthesis with latent diffusion models. In *Proceedings of the IEEE/CVF conference on computer vision and pattern recognition*, pages 10684–10695, 2022.
- [56] Olaf Ronneberger, Philipp Fischer, and Thomas Brox. U-net: Convolutional networks for biomedical image segmentation. In *Medical image computing and computer-assisted intervention–MICCAI 2015: 18th international conference, Munich, Germany, October 5-9, 2015, proceedings, part III 18*, pages 234–241. Springer, 2015.
- [57] Aditya Sanghi, Hang Chu, Joseph G Lambourne, Ye Wang, Chin-Yi Cheng, Marco Fumero, and Kamal Rahimi Malekshan. Clip-forge: Towards zero-shot text-to-shape generation. In *Proceedings of the IEEE/CVF Conference on Computer Vision and Pattern Recognition*, pages 18603–18613, 2022.
- [58] Fulvio Scarano. Tomographic piv: principles and practice. *Measurement Science and Technology*, 24(1):012001, 2012.
- [59] Daniel Schanz, Sebastian Gesemann, and Andreas Schröder. Shake-the-box: Lagrangian particle tracking at high particle image densities. *Experiments in fluids*, 57:1–27, 2016.
- [60] Ruoxi Shi, Hansheng Chen, Zhuoyang Zhang, Minghua Liu, Chao Xu, Xinyue Wei, Linghao Chen, Chong Zeng, and Hao Su. Zero123++: a single image to consistent multi-view diffusion base model. *arXiv preprint arXiv:2310.15110*, 2023.
- [61] Jascha Sohl-Dickstein, Eric Weiss, Niru Maheswaranathan, and Surya Ganguli. Deep unsupervised learning using nonequilibrium thermodynamics. In *International conference on machine learning*, pages 2256–2265. PMLR, 2015.
- [62] Yang Song, Jascha Sohl-Dickstein, Diederik P Kingma, Abhishek Kumar, Stefano Ermon, and Ben Poole. Score-based generative modeling through stochastic differential equations. *arXiv preprint arXiv:2011.13456*, 2020.

- [63] Kimberly Stachenfeld, Drummond B Fielding, Dmitrii Kochkov, Miles Cranmer, Tobias Pfaff, Jonathan Godwin, Can Cui, Shirley Ho, Peter Battaglia, and Alvaro Sanchez-Gonzalez. Learned coarse models for efficient turbulence simulation. *arXiv e-prints*, pages arXiv–2112, 2021.
- [64] Makoto Takamoto, Timothy Praditia, Raphael Leiteritz, Daniel MacKinlay, Francesco Alesiani, Dirk Pflüger, and Mathias Niepert. Pdebench: An extensive benchmark for scientific machine learning. *Advances in Neural Information Processing Systems*, 35:1596–1611, 2022.
- [65] Jiapeng Tang, Jiabao Lei, Dan Xu, Feiying Ma, Kui Jia, and Lei Zhang. Saccovnet: Sign-agnostic optimization of convolutional occupancy networks. In *Proceedings of the IEEE/CVF International Conference on Computer Vision*, pages 6504–6513, 2021.
- [66] Jonathan Tompson, Kristofer Schlachter, Pablo Sprechmann, and Ken Perlin. Accelerating eulerian fluid simulation with convolutional networks. In *International conference on machine learning*, pages 3424–3433. PMLR, 2017.
- [67] Alasdair Tran, Alexander Mathews, Lexing Xie, and Cheng Soon Ong. Factorized fourier neural operators. In *The Eleventh International Conference on Learning Representations*.
- [68] Edgar Tretschk, Ayush Tewari, Vladislav Golyanik, Michael Zollhöfer, Carsten Stoll, and Christian Theobalt. Patchnets: Patch-based generalizable deep implicit 3d shape representations. In *Computer Vision—ECCV 2020: 16th European Conference, Glasgow, UK, August 23–28, 2020, Proceedings, Part XVI 16*, pages 293–309. Springer, 2020.
- [69] Arash Vahdat, Francis Williams, Zan Gojcic, Or Litany, Sanja Fidler, Karsten Kreis, et al. Lion: Latent point diffusion models for 3d shape generation. *Advances in Neural Information Processing Systems*, 35:10021–10039, 2022.
- [70] Ashish Vaswani, Noam Shazeer, Niki Parmar, Jakob Uszkoreit, Llion Jones, Aidan N Gomez, Łukasz Kaiser, and Illia Polosukhin. Attention is all you need. *Advances in neural information processing systems*, 30, 2017.
- [71] Ricardo Vinuesa and Steven L Brunton. Enhancing computational fluid dynamics with machine learning. *Nature Computational Science*, 2(6):358–366, 2022.
- [72] Ricardo Vinuesa, Steven L Brunton, and Beverley J McKeon. The transformative potential of machine learning for experiments in fluid mechanics. *Nature Reviews Physics*, 5(9):536–545, 2023.
- [73] Vikram Voleti, Chun-Han Yao, Mark Boss, Adam Letts, David Pankratz, Dmitry Tochilkin, Christian Laforte, Robin Rombach, and Varun Jampani. Sv3d: Novel multi-view synthesis and 3d generation from a single image using latent video diffusion, 2024. URL <https://arxiv.org/abs/2403.12008>.
- [74] Nils Wandel, Michael Weinmann, and Reinhard Klein. Learning incompressible fluid dynamics from scratch-towards fast, differentiable fluid models that generalize. In *International Conference on Learning Representations*.

- [75] Mustafa Z Yousif and Hee-Chang Lim. Reduced-order modeling for turbulent wake of a finite wall-mounted square cylinder based on artificial neural network. *Physics of Fluids*, 34(1), 2022.
- [76] Mustafa Z Yousif, Linqi Yu, Sergio Hoyas, Ricardo Vinuesa, and HeeChang Lim. A deep-learning approach for reconstructing 3d turbulent flows from 2d observation data. *Scientific Reports*, 13(1):2529, 2023.
- [77] Zehao Yu, Anpei Chen, Binbin Huang, Torsten Sattler, and Andreas Geiger. Mip-splatting: Alias-free 3d gaussian splatting. In *Proceedings of the IEEE/CVF Conference on Computer Vision and Pattern Recognition*, pages 19447–19456, 2024.
- [78] Biao Zhang, Matthias Nießner, and Peter Wonka. 3dilg: Irregular latent grids for 3d generative modeling. *Advances in Neural Information Processing Systems*, 35: 21871–21885, 2022.
- [79] Biao Zhang, Jiapeng Tang, Matthias Niessner, and Peter Wonka. 3dshape2vecset: A 3d shape representation for neural fields and generative diffusion models. *ACM Transactions on Graphics (TOG)*, 42(4):1–16, 2023.